Evaluation of Polar Winter Mesopause Wind in WACCMX+DART

V. Lynn Harvey[1,2] [ID], **Nick Pedatella[3]** [ID], **Erich Becker[4]** [ID], **and Cora Randall[1,2]** [ID]

[1]Laboratory for Atmospheric and Space Physics, University of Colorado, Boulder, CO, USA, [2]Atmospheric and Oceanic Sciences Department, University of Colorado, Boulder, CO, USA, [3]National Center for Atmospheric Research, High Altitude Observatory, Boulder, CO, USA, [4]NorthWest Research Associates, Boulder, CO, USA

Abstract This work evaluates zonal winds in both hemispheres near the polar winter mesopause in the Whole Atmosphere Community Climate Model (WACCM) with thermosphere-ionosphere eXtension combined with data assimilation using the Data Assimilation Research Testbed (DART) (WACCMX+DART). We compare 14 years (2006–2019) of WACCMX+DART zonal mean zonal winds near 90 km to zonal mean zonal winds derived from Sounding of the Atmosphere using Broadband Emission Radiometry (SABER) geopotential height measurements during Arctic mid-winter. 10 years (2008–2017) of WACCMX+DART zonal mean zonal winds are compared to SABER in the Antarctic mid-winter. It is well known that WACCM, and WACCM-X, zonal winds at the polar winter mesopause exhibit a strong easterly (westward) bias. One explanation for this is that the models omit higher order gravity waves (GWs), and thus the eastward drag caused by these GWs. We show for the first time that the model winds near the polar winter mesopause are in closer agreement with SABER observations when the winds near the stratopause are weak or reversed. The model and observed mesosphere and lower thermosphere winds agree most during dynamically disturbed times often associated with minor or major sudden stratospheric warming events. Results show that the deceleration of the stratospheric and mesospheric polar night jet allows enough eastward GWs to propagate into the mesosphere, driving eastward zonal winds that are in agreement with the observations. Thus, in both hemispheres, the winter polar night jet speed and direction near the stratopause may be a useful proxy for model fidelity in the polar winter upper mesosphere.

1. Introduction

Many science topics require accurate simulation of neutral winds in the mesosphere and lower thermosphere (MLT). To name a few, studies involving atmospheric tides, planetary waves (PWs) and gravity waves (GWs) need neutral wind information because the background winds through which these waves propagate impact wave characteristics. Thus, knowledge of the neutral winds is important for studying thermosphere–ionosphere variability driven by waves propagating up from below (e.g., Akmaev, 2011; Liu, 2016; Vincent, 2015). It is also necessary to have accurate knowledge of the winds at high spatial and temporal resolution to fully understand the transport of constituents. For example, large horizontal and vertical wind shears (e.g., Larsen, 2002; Liu, 2007) affect the transport of space shuttle water vapor (e.g., Datta-Barua et al., 2021; Yue et al., 2013), which has been linked to variability in polar mesospheric clouds (e.g., Stevens et al., 2014). In addition to accurate knowledge of the composition, accurate neutral winds would aid in understanding how the residual circulation in the upper mesosphere (Holton, 1983) interacts with an opposing global circulation in the lower thermosphere that is simulated in models (Smith et al., 2011) and how this interaction may vary as a function of local time, season, and solar cycle. Finally, accurate winds in the MLT would support studies to clarify long-standing uncertainties in the descent of energetic particle precipitation-produced nitrogen oxides in the mesospheric polar vortex (e.g., Meraner & Schmidt, 2016; Randall et al., 2015).

Given the dearth of accurate, global wind observations at MLT altitudes, we often use whole atmosphere models to understand the physics of wave propagation and dissipation, global and regional circulations, and constituent transport. One of the most widely used models is the Whole Atmosphere Community Climate Model (WACCM) (Marsh et al., 2013). Unfortunately, there is a limitation to using WACCM as a tool to study these processes in the polar winter mesopause region because it has a well-known easterly (westward) wind bias in the polar winter upper mesosphere (e.g., Eswaraiah et al., 2016; Harvey et al., 2019; Hindley et al., 2022; Lieberman et al., 2015; Liu, 2016; Marsh et al., 2013; Noble et al., 2022; Rüfenacht et al., 2018; Smith, 2012; Yuan et al., 2008; Zhang

Writing – review & editing: V. Lynn
Harvey, Nick Pedatella, Erich Becker,
Cora Randall

et al., 2021). This bias is not unique to WACCM, and other comprehensive high-top general circulation models with parameterized GWs show the same deficiencies in simulating the observed zonal wind structure (e.g., Wilhelm et al., 2019) in the winter upper mesosphere (e.g., Griffith et al., 2021; McCormack et al., 2017, 2021; McLandress et al., 2006; Pedatella, Fuller-Rowell, et al., 2014; Schmidt et al., 2006). However, not all high-top models exhibit the easterly wind bias to the same degree. Several notable effects of the easterly wind bias are (a) to reduce the vertical extension of the mesospheric polar vortex (Harvey et al., 2019), (b) to increase the vertical wind shear, which promotes dynamic instability and the growth of PWs (e.g., Chandran et al., 2013; France et al., 2015), (c) to drive a persistent region of negative meridional potential vorticity gradients at mid-to-high latitudes, which gives rise to the generation of PWs via baroclinic or barotropic instability (e.g., Charney & Stern, 1962), and (d) to reduce the amplitude of the migrating semidiurnal tide with wavenumber 2 in the Arctic winter (Zhang et al., 2021).

Models are generally run in three different modes: free-running, specified dynamics, or with data assimilation. Free-running models are unconstrained throughout their domains and rely solely on input boundary conditions and model physics to predict the atmospheric state. Specified dynamics mode relaxes (or "nudges") the model dynamics to meteorological reanalysis data over a given altitude range, thus enabling comparisons to observations on any given day. See Froidevaux et al. (2019) for a detailed discussion of free-running versus specified dynamics simulations. Data assimilation mode is an alternative to specified dynamics to enable day-to-day comparisons to observations (e.g., Pedatella et al., 2013). In this mode model chemistry and/or dynamics are directly constrained by assimilating ground-based, suborbital, and satellite observations. When running in specified-dynamics mode, high-top models like WACCM have been shown to exhibit superior performance when the nudging region extends to mesopause altitudes, compared to nudging only up to the stratopause (e.g., Pedatella, Liu, et al., 2018; Sassi et al., 2018; Siskind et al., 2015). However, most meteorological reanalyses do not extend to these altitudes. Pedatella, Liu, et al. (2018) demonstrated better agreement between modeled and observed descent of NO_x when the model was constrained by observations in the mesosphere in using data assimilation versus specified dynamics nudging to the stratopause by reanalysis data. Sassi et al. (2018) showed that constraining the model mesosphere resulted in more realistic thermospheric variability compared to only nudging up to the stratopause. They found that nudging to mesopause altitudes improved comparisons between simulated and observed distributions of carbon monoxide. And Siskind et al. (2015) showed much better agreement between modeled and observed NO and methane distributions when WACCM was nudged to the Navy Operational Global Atmospheric Prediction System-Advanced Level Physics High Altitude (NOGAPS-ALPHA) in the mesosphere versus nudging only up to the stratopause. They hypothesized that constraining WACCM in the mesosphere "compensates for an underestimate of nonorographic GW drag" in the model. This is consistent with Smith et al. (2017), who demonstrated that when the nudging extends only up to the stratopause, the free-running mesosphere diverges from a previous simulation that served as "truth" and the degree of divergence depends on non-orographic GW properties.

Recently, Hindley et al. (2022) compared WACCM winds to meteor radar-derived zonal winds near South Georgia Island in the Southern Hemisphere (SH). They hypothesize that the easterly model wind bias in the MLT "could be due to an incomplete representation of drag due to GWs, in particular secondary GWs." This hypothesis was based on the study of Becker and Vadas (2018), who showed that the easterly wind bias for strong polar vortex conditions is eliminated when GWs are simulated explicitly. They also showed that there is a significant eastward drag from secondary GWs in the winter MLT that is absent when GWs are parameterized. Harvey et al. (2019) hypothesized that the easterly wind bias is due to either too strong westward GW drag by non-orographic GWs, missing eastward GW drag in the upper mesosphere from secondary GWs, or both. Indeed, the seasonally averaged zonal wind structure in Sounding of the Atmosphere Using Broadband Emission Radiometry (SABER) shown by Harvey et al. (2019) resembles the zonal winds in the GW-resolving model used by Becker and Vadas (2018, see their Figure 2) in which much of the relevant GW spectrum is resolved. This suggests that missing eastward forcing from secondary GWs is an important reason for the easterly wind bias in coarse-resolution, high-altitude models.

Previous studies have documented the model easterly wind bias in monthly or seasonal means. This work is the first to quantify sub-seasonal and interannual variability in the easterly model wind bias in the polar winter upper mesosphere, namely that it is reduced, and even eliminated when conditions in the stratosphere are dynamically disturbed. This paper is organized as follows. Section 2 describes the model framework and simulations and the

satellite observations used to evaluate the model. Section 3 presents a case study that demonstrates sub-seasonal variations in model fidelity in the upper mesosphere before, during, and after the major sudden stratospheric warming (SSW) in 2006. Section 4 presents daily variations in the model zonal wind bias in the polar upper mesosphere in both hemispheres for multiple years. Section 5 discusses the mechanisms involved in driving the model zonal wind bias and variations therein. Section 6 summarizes the results and gives future directions.

2. WACCMX+DART

2.1. Model Description

Whole Atmosphere Community Climate Model with thermosphere-ionosphere eXtension WACCMX (WACCMX) is a general circulation model that extends from the Earth's surface to ~500 km and simulates relevant processes from the troposphere to the thermosphere and ionosphere (Liu et al., 2018). These include major-species diffusive transport, ion drag, Joule heating, non-local thermodynamic equilibrium, and ionospheric physics and chemistry. The WACCMX configuration used here (see Pedatella et al., 2013; Pedatella, Raeder, et al., 2014) employs the Data Assimilation Research Testbed (DART) ensemble adjustment Kalman filter (Anderson, 2001) to constrain model meteorology up to ~100 km.

For the present study, WACCMX+DART assimilated conventional meteorological observations (i.e., radiosonde temperature and winds, satellite-based cloud drift winds, and aircraft observations) in the troposphere, refractivity from GPS radio occultation in the troposphere and stratosphere, and SABER and Microwave Limb Sounder (MLS) temperature observations from ~20 to ~100 km. Since MLS and SABER temperatures are assimilated, a comparison of model output to SABER is not an entirely independent evaluation. However large differences between WACCMX+DART winds and those derived from SABER observations (shown in Sections 3 and 4) suggest that the modeled zonal mean zonal winds are only loosely constrained in the upper mesosphere. The weak constraint on the zonal mean zonal winds in WACCMX+DART results from the sparseness of the temperature observations that are assimilated in the mesosphere. It may also be related to inadequate representation of the multi-variate cross-covariance between temperature and zonal wind, which will impact the degree to which temperature observations are able to adjust the zonal wind through data assimilation.

Subgrid-scale GWs are parameterized in the model. Orographic GWs are accounted for using the formulation of McFarlane (1987). Richter et al. (2010) describe how the addition of surface stress due to unresolved topography yields more realistic stratospheric variability in the Arctic. Non-orographic GWs are generated by convective processes (Beres et al., 2005) and fronts (Richter et al., 2010). Richter et al. (2010) describe how non-orographic GWs are launched in the model when a frontogenesis threshold at 600 hPa is met. When this happens, a spectrum of GWs emanates from intermittent frontal sources, and has phase speeds ranging from −80 to +80 m/s every 2.5 m/s. GWs generated by shear instabilities, such as in jet exit regions (e.g., Fritts & Luo, 1992) or by the stratospheric polar vortex (e.g., Sato & Yoshiki, 2008), are currently unaccounted for. The turbulent Prandtl number that governs thermal diffusion is set to Pr = 2 as suggested by Garcia et al. (2014). These parameterizations can be tuned based on the scientific application. For example, Smith-Johnsen et al. (2022) decreased the Prandtl number to 1, which acted to increase eddy diffusion and led to better agreement with Solar Occultation For Ice Experiment satellite measurements of NO in the MLT. They also reduced the amplitude of non-orographic GWs and, because they then broke at higher altitudes, found better agreement with observations in both winter NO_x descent and in the altitude of the summer mesopause. GWs parameterizations currently used in global climate models such as WACCM are subject to severe limitations that are implied by for example, single-column and steady-state approximations (e.g., Becker, 2017; Senf & Achatz, 2011). Indeed, studies show significant oblique GW propagation including into the polar mesosphere region (e.g., Alexandre et al., 2021), and examine the associated drag that such waves would add to a model such as WACCMX+DART (e.g., Kalisch et al., 2014). Further, the assumption that the GWs that affect the winter upper mesosphere have tropospheric sources was questioned in recent studies about secondary GWs (Becker & Vadas, 2018; Vadas & Becker, 2018).

The model horizontal resolution is 1.9° × 2.5° in latitude × longitude. The model vertical resolution increases with altitude as follows: ~100 m in the planetary boundary layer, ~1 km near 3 km altitude, ~2 km near 50 km, ~3 km near 110 km, and ~10 km near 400 km. Horizontal wind and geopotential height (GPH) fields are output hourly, from which daily averages are computed. Simulations were run from 20 December to 20 March in each Arctic winter from 2005/2006 to 2018/2019 for comparison to the northward-looking SABER yaw in the

Table 1
Arctic SSW Date Ranges, Major or Minor Classifications, Types, Duration, and NH/SH SABER Yaw Dates for the Years 2006–2019.

YEAR	Arctic SSW Date Range	WMO Defn.	Type*	SSW Length	SABER NH Winter Yaw	SABER SH Winter Yaw
2006	Jan 21-Feb 15	Major	D	26	Jan 14 – Mar 16	July 15 – Sep 17
2007	Feb 4-7	Minor	D	4	Jan 13 – Mar 15	July 16 – Sep 16
	Feb 24-27	Major	D	4		
2008	Jan 23-27	Minor	D	5	Jan 13 – Mar 14	July 13 – Sep 15
	Feb 5-9	Minor	D	5		
	Feb 13-18	Minor	D	6		
	Feb 22-28	Major	D	7		
2009	Jan 24-Feb 22	Major	S	30	Jan 12 – Mar 15	July 13 – Sep 15
2010	Jan 21-Feb 3	Minor	D	14	Jan 11 – Mar 15	July 12 – Sep 14
	Feb 9-23	Major	S	15		
2011	Jan 31-Feb 3	Minor	D	4	Jan 10 – Mar 14	July 11 – Sep 13
2012	Jan 12-Feb 1	Minor	D	21	Jan 9 – Mar 12	July 10 – Sep 12
2013	Jan 7-27	Major	S	21	Jan 7 – Mar 11	July 9 – Sep 11
2014	Feb 7-10	Minor	S	4	Jan 6 – Mar 10	July 8 – Sep 9
	Feb 19-22	Minor	D	4		
	Mar 1-10	Minor	D	10		
2015	Jan 14-29	Minor	D	16	Jan 5 – Mar 9	July 6 – Sep 8
	Feb 6-11	Minor	D	6		
2016	Jan 30-Feb 2	Minor	D	4	Jan 4 - Mar 6	July 2 – Sep 4
	Feb 7-13	Minor	D	7		
2017	Jan 27-Feb 8	Minor	D	13	Jan 1 – Mar 2	July 1 – Sep 2
	Feb 22-Mar 3	Minor	D	10		
2018	Feb 12-28	Major	S	17	Dec 30 – Mar 1	June 29–Aug 30
2019	Jan 2-21	Major	S	20	Dec 28 – Feb 26	June 27-Aug 28
***D = Polar Vortex Displacement *S = Polar Vortex Split**						

Note. Northern Hemisphere (NH); Southern Hemisphere (SH); Sounding of the Atmosphere Using Broadband Emission Radiometry (SABER); Sudden Stratospheric Warming (SSW).

Northern Hemisphere (NH) winter. SH simulations were run from 20 June to 20 September of each Antarctic winter from 2008 to 2017 for comparison to the southward-looking SABER yaw in the SH winter. SH winter simulations were performed separately from the NH winter simulations to minimize computational cost. More NH winters than originally intended are included here to capture the major SSWs in January 2006, February 2018, and January 2019. The simulations were initialized on 1 December for the NH winters and 1 June for the SH winters using initial conditions from a transient historical run. This resulted in 20 days of spin-up time for each run. For each simulation, small perturbations were added to the initial temperature and wind fields to generate 40 ensemble members. The perturbations are obtained by adding a random value, which is obtained by sampling a Gaussian distribution with zero mean and 0.001 standard deviation, to the initial conditions at each model grid point. This work compares the model ensemble means to observations. See Table 1 for SABER yaw dates that overlap with each of these simulations and dictate which days are analyzed in each year and hemisphere. Note, SABER SH yaw dates in 2006, 2007, 2018, and 2019 are not analyzed since they are outside the time of the simulations. Table 1 also lists Arctic SSW date ranges, classifications (major vs. minor), types (split vs. displacement), and durations for the years considered here. The duration of each SSW is the total number of days, as given by the date range, during which the SSW definition is satisfied. Minor SSWs are defined when the 10 hPa zonal mean temperature at the pole exceeds that at 60° latitude, and 10 hPa zonal mean zonal winds at 60° latitude remain westerly. Major SSWs are defined to occur when 10 hPa zonal mean zonal winds at 60° latitude
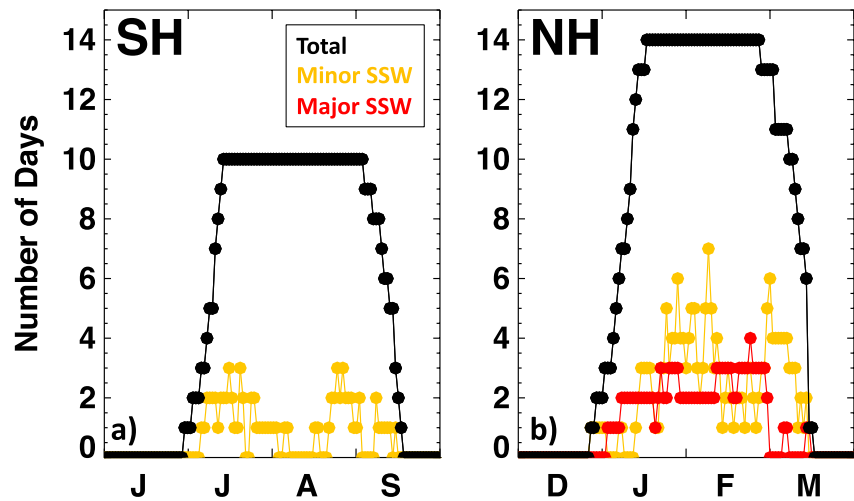
Figure 1. The total number of days included in this study (black) for each day of the year and hemisphere. (a) Days from June to September are analyzed in the Southern Hemisphere (SH). (b) Days from December-March are analyzed in the Northern Hemisphere (NH). The total number of minor and major sudden stratospheric warming (SSW) days are shown in yellow and red, respectively.

are easterly (e.g., Butler et al., 2015 and references therein). Onset dates for major SSWs are in agreement with Butler et al. (2017). Figure 1 illustrates the total number of days included in this study (black line with black dots) for each day of the year in each hemisphere. The total numbers of minor and major SSW days for each day of the year in each hemisphere are given in yellow and red, respectively.

2.2. Model Evaluation

In this work SABER satellite data are used to evaluate the accuracy of zonal winds in the model polar winter MLT. SABER is a 10-channel limb-scanning infrared radiometer that measures atmospheric 15-μm CO_2 emission, from which kinetic temperature is retrieved (Russell et al., 1999). Profiles of GPH are derived from the temperature and pressure assuming hydrostatic balance (see Remsberg et al., 2008 for more details). On each day the SABER latitude coverage extends from 82°S to 53°N or 53°S to 82°N depending on the ~60-day spacecraft yaw cycle. Comparisons to WACCMX+DART in each hemisphere include only those days when SABER observed the entire hemisphere, as indicated in Table 1. Local time sampling precesses such that all local times are observed over the course of about 60 days. In this work we use version 2.0 temperature and GPH data. Temperature profiles have 2 km vertical resolution and estimates of precision are less than 4 K throughout the mesosphere (García-Comas et al., 2008; Remsberg et al., 2003).

SABER irregularly spaced profile data are gridded twice per day using a spatial Delaunay triangulation (Knuth, 1992, and references therein) to generate near-global maps at the horizontal resolution of the model and the native vertical resolution of the instrument. Ascending and descending node data (both of which provide global coverage) are gridded separately and are then averaged to minimize diurnal tidal variations in the upper mesosphere. We then calculate geostrophic winds using the gridded GPH fields (e.g., Holton, 2004, Equation 3.11). Zonal mean zonal winds are estimated to have a precision of 2 m/s at 0.01 hPa (~80 km). Geostrophic zonal and meridional winds are computed from WACCMX+DART GPH fields for an apples-to-apples comparison to winds derived from SABER. Zonal mean geostrophic zonal winds are generally within 2 m/s (or ~10%) of zonal mean full vector winds at 0.001 hPa (~90 km) averaged poleward 40°N. Since in this work we analyze daily zonally averaged zonal winds in broad latitude bands, the geostrophic wind approximation is sufficient to accurately quantify the model easterly wind bias in the polar winter MLT. Figure 2 shows zonal mean geostrophic zonal wind profiles in the model (red) and in SABER (black) averaged over all days considered in each hemisphere. The magnitude of the model easterly wind bias relative to SABER in the mesosphere and the larger easterly bias in the SH compared to in the NH are both in good agreement with previous monthly or seasonally averaged estimates (e.g., Smith, 2012). The fact that the easterly zonal wind bias is larger in the SH than in the NH is consistent with the notion that the effects of secondary GWs in the winter MLT are larger in the SH than
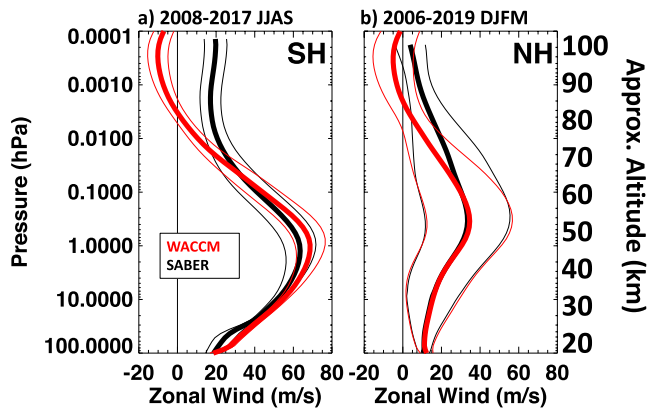
Figure 2. Zonal mean zonal wind profiles in Sounding of the Atmosphere using Broadband Emission Radiometry (SABER) (black) and WACCMX+DART (red) poleward of 40° latitude in (a) the Southern Hemisphere (SH) and (b) the Northern Hemisphere (NH). In the SH winds are averaged over all June, July, August, and September days from 2008 to 2017 in which SABER viewed the entire SH. In the NH winds are averaged over all December, January, February, and March days from 2006 to 2019 in which SABER viewed the entire NH. Thin lines give one standard deviation about the mean. The winds from both SABER and WACCMX+DART are computed as described in the text.

in the NH (Becker et al., 2020), but are missing in WACCMX+DART. For the remainder of this work we focus on time variations in the model easterly wind bias in the winter MLT.

3. 2006 Case Study

We first demonstrate sub-seasonal time variations in the model easterly wind bias during a case study that takes place before, during, and after the Arctic 2006 major SSW. Figure 3 shows monthly mean polar maps of geostrophic zonal winds at 0.001 hPa (~90 km) in January 2006 (top) and February 2006 (bottom). WACCMX+DART is on the left, SABER is in the middle, and differences are given on the right. Monthly means for January 2006 show the model zonal winds to be in reasonable agreement with the observations. But in February 2006 there are strong circumpolar easterlies in the model that are not observed. This analysis demonstrates that the easterly wind bias in the model is not constant in time. But when and why do the simulated and observed winds diverge?

Answering the question just posed requires examining the meteorology during this case. Figure 4 gives altitude-time sections of stratospheric and mesospheric temperature (top), zonal wind (middle), and PW amplitudes (bottom) in WACCMX+DART during January and February 2006. During this time, meteorological conditions in the stratosphere and mesosphere were as follows. There was a major SSW with an onset date of 21 January 2006, with associated descent and warming of the stratopause and cooling in the mesosphere, a reversal of the zonal winds at 10 hPa, and large PWs in the stratosphere and mesosphere before SSW onset and weak PWs after SSW onset. The major SSW on 21 January followed a similar disturbance about a week earlier; and while the zonal winds in the upper stratosphere and lower mesosphere (USLM, ~40–60 km) reversed on 13 January, this wind reversal did not extend down to the 10 hPa level (~30 km) where SSWs are defined. Westerly winds and large PWs from 80 to 100 km follow both stratospheric wind reversals as a result of GW filtering and dissipation processes (Lieberman et al., 2013; Smith, 1996, 1997). Following this major displacement-type SSW the polar stratopause became ill-defined and reformed near 80 km. In early-mid February the polar night jet in the upper stratosphere returned to westerly and the amplitude of quasi-stationary PWs subsided. See Manney et al. (2008) for a more detailed description of the meteorology during this time.

Figure 5 presents timeseries of zonal mean zonal wind at 0.001 hPa (~90 km) in WACCMX+DART (black) and SABER (gray) to illustrate exactly when the two diverge. We also compare WACCMX+DART and SABER GPH maps at 0.001 hPa to better understand the synoptic meteorology before and after the model and observed MLT winds diverge. The top panel shows good agreement between simulated and observed winds from 13 to 29 January. During this time minor SSW criteria were satisfied from 13 to 18 January and major SSW criteria were met on 21 January. After 29 January the simulated and observed winds diverge despite the persistence of the major SSW to mid-February. It will be shown that the degree to which the model and observations agree is best predicted by the zonal winds near the stratopause, not at 10 hPa. The middle and bottom rows show a sequence of polar GPH maps on three select days illustrating the geographic location of high and low pressure systems in the upper mesosphere before and after the simulated and observed zonal winds diverge. Note, there is good agreement between simulated and observed GPH maps throughout the stratosphere and lower mesosphere on all days (not shown). On 24 January when zonal winds in the USLM are weak westerly or easterly (Figure 4b), the model and SABER GPH maps are in general agreement in the polar upper mesosphere. In particular, in late January both the model and the observations show a low pressure center at polar latitudes. However, by 1 February when the zonal winds in the USLM are strong westerly, polar maps of GPH disagree between WACCMX+DART and SABER. Between 1 and 10 February the circumpolar cyclone in the model turns into an anticyclone that is not borne out by the observations. This scenario occurs repeatedly in different years of the simulation. That is, the level of agreement between the model and observations depends on the sign and strength of the winds in the USLM. During dynamically disturbed times often associated with either minor or major SSWs, both the model and observations show a deepening cyclone in the upper mesosphere that migrates around the hemisphere. But
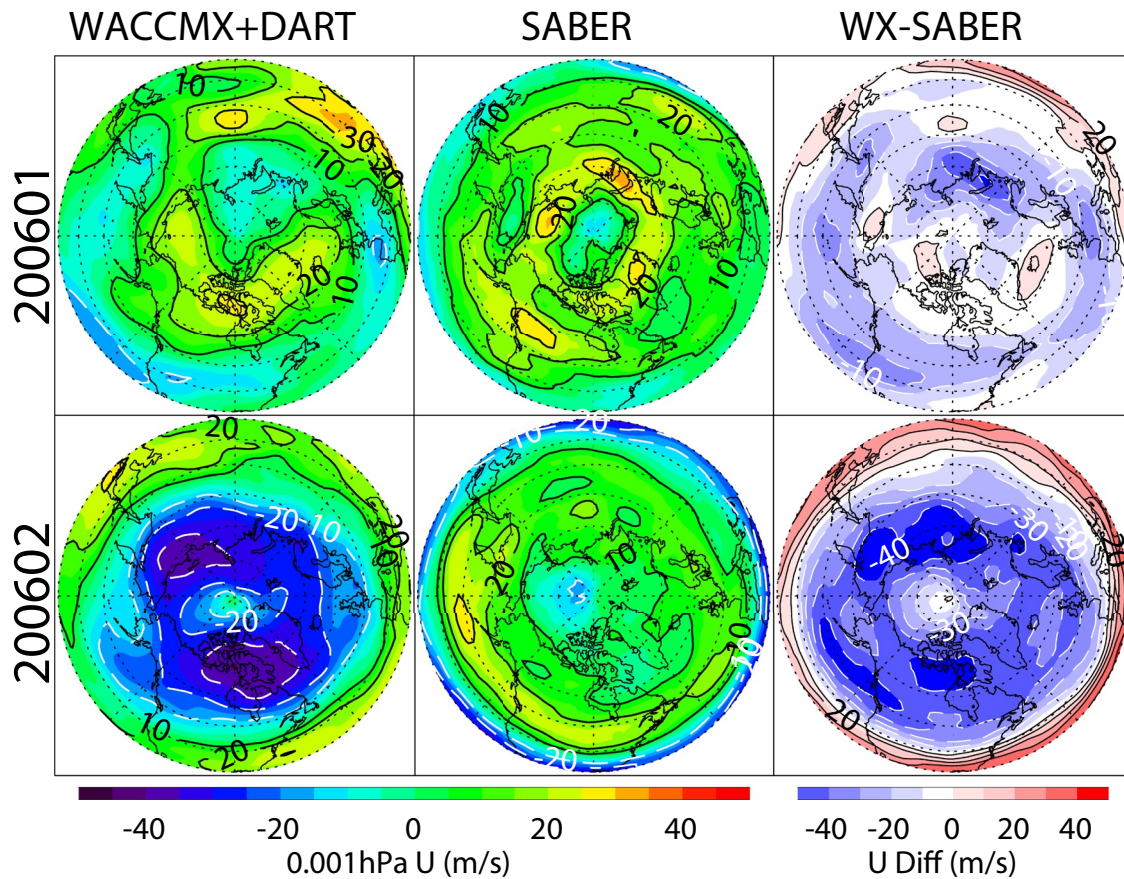
Figure 3. Northern Hemisphere polar plots of monthly mean geostrophic zonal winds calculated from WACCMX+DART geopotential height (GPH) (left), from Sounding of the Atmosphere using Broadband Emission Radiometry (SABER) GPH (middle), and the differences (WACCMX+DART minus SABER, right). Geostrophic zonal winds and differences are shown at 0.001 hPa (~90 km) in January 2006 (top) and February 2006 (bottom).

during undisturbed times, whether prior to an SSW or upon recovery from an SSW, the observations suggest that a circumpolar cyclone exists over the pole in the winter upper mesosphere while the model simulates a circumpolar anticyclone.

4. Climatology of Model-Measurement Zonal Wind Differences

In this section, we show the daily evolution of modeled and observed zonal winds over multiple years. These results demonstrate for the first time that the model easterly wind bias exhibits large sub-seasonal and interannual variations.

4.1. Northern Hemisphere Winter

Figure 6 shows 14 January–March segments for each year from 2006 to 2019 of WACCMX+DART (black with diamonds) and SABER (gray) daily averaged zonal mean zonal winds at 0.001 hPa averaged poleward of 40°N for all days (897) in which SABER observed the NH. This broad latitude band average allows jets to be located at slightly different latitudes in the model versus in SABER and still be a reliable measure of whether there is a cyclone (with westerly winds in midlatitudes) or an anticyclone (with easterly winds in midlatitudes) over the pole in the model. Major SSW days (136) are in red and minor SSW days (198) are in yellow. WACCMX+DART and SABER zonal winds are uncorrelated ($r = 0.11$) based on all days at this altitude. That the black line is often negative (easterly mean winds) while the gray line largely remains positive reflects the easterly model wind bias. However, there is large variability in the sign of the simulated zonal winds in the upper mesosphere from day-to-day and from year-to-year. In general, WACCMX+DART zonal winds tend to exhibit an easterly wind bias on
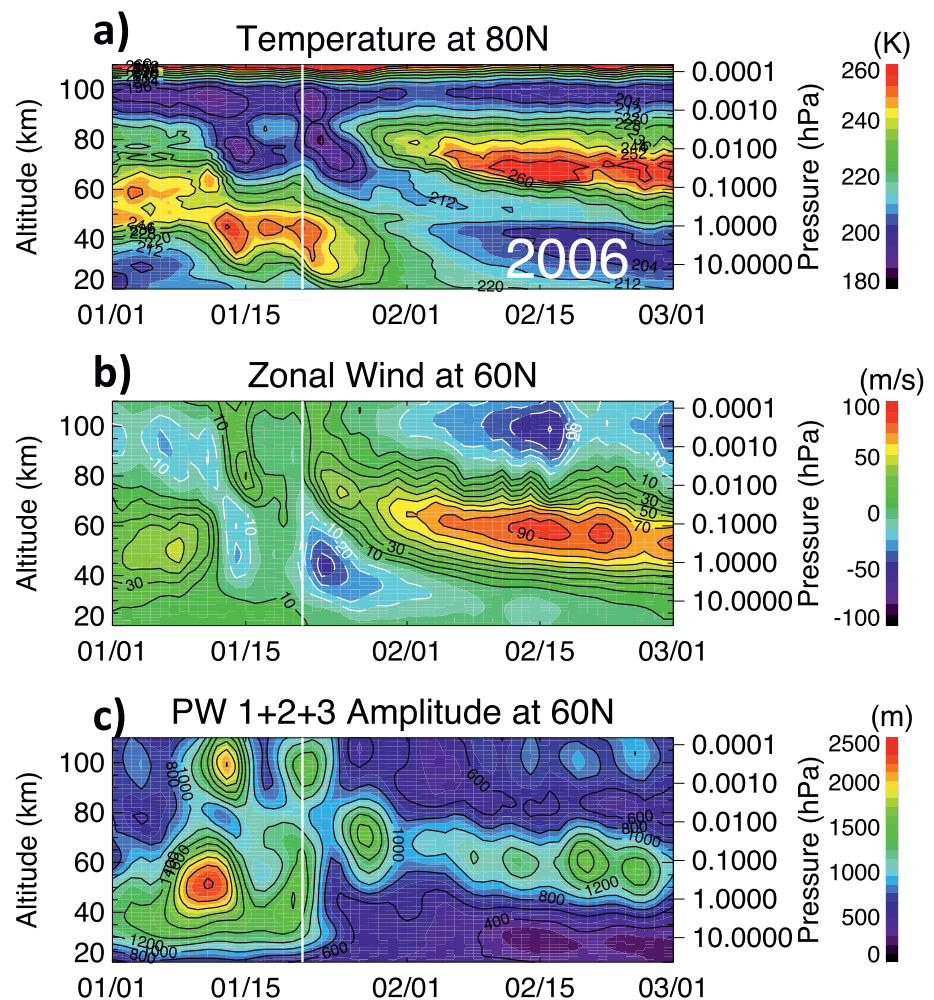
Figure 4. Altitude-time plots from 1 January through 1 March 2006 and from 20 to 110 km of WACCMX+DART (a) zonal mean temperature at 80°N, (b) zonal mean zonal wind at 60°N, and (c) planetary wave (PW) amplitude (for waves 1, 2, and 3 combined) at 60°N. The vertical white lines denote 21 January, the onset of a major sudden stratospheric warming.

non-SSW days. Simulated zonal winds are usually westerly and in better agreement with the observations during dynamically disturbed times, except in the weeks following the onset of the prolonged major SSWs in 2006, 2009, 2013, and 2019 (i.e., Orsolini et al., 2017; Pérot & Orsolini, 2021; Siskind et al., 2010). In the first week or so following major SSW onset the modeled and observed zonal winds in the MLT are both westerly and in good agreement, as is the case during most minor SSWs. Zhang et al. (2021) also found improved agreement between high latitude zonal winds simulated by SD-WACCM-X and observed by radars in the first 2 weeks following SSW onset. However, as these particular major SSWs persist, the model winds in the MLT turn easterly after about 10 days but remain westerly in the observations. Thus the fidelity of MLT winds in the model improves early during SSWs, but regresses during the prolonged stage of SSWs. That is, highly disturbed dynamical conditions in the stratosphere are favorable for simulating MLT winds by WACCMX+DART with the current GW physics, but conditions during dynamically quiet times or SSW recoveries are more problematic. Note, we similarly evaluated polar cap (60–90° latitude) average temperature in the model upper mesosphere and results (not shown) indicate that the well-known ~10 K warm bias in the winter upper mesosphere of WACCM (e.g., Harvey et al., 2019; Marsh et al., 2013; Smith, 2012) also varies with time, consistent with the time variations in the easterly wind bias. In other words, the model warm bias persists when the vortex is strong while mesospheric coolings during SSWs are accurately simulated.

Figure 6 emphasizes the model-measurement agreement in the context of minor and major SSWs, which as noted above are defined by temperatures and winds at 10 hPa. However, SSW-induced variability in the mesosphere
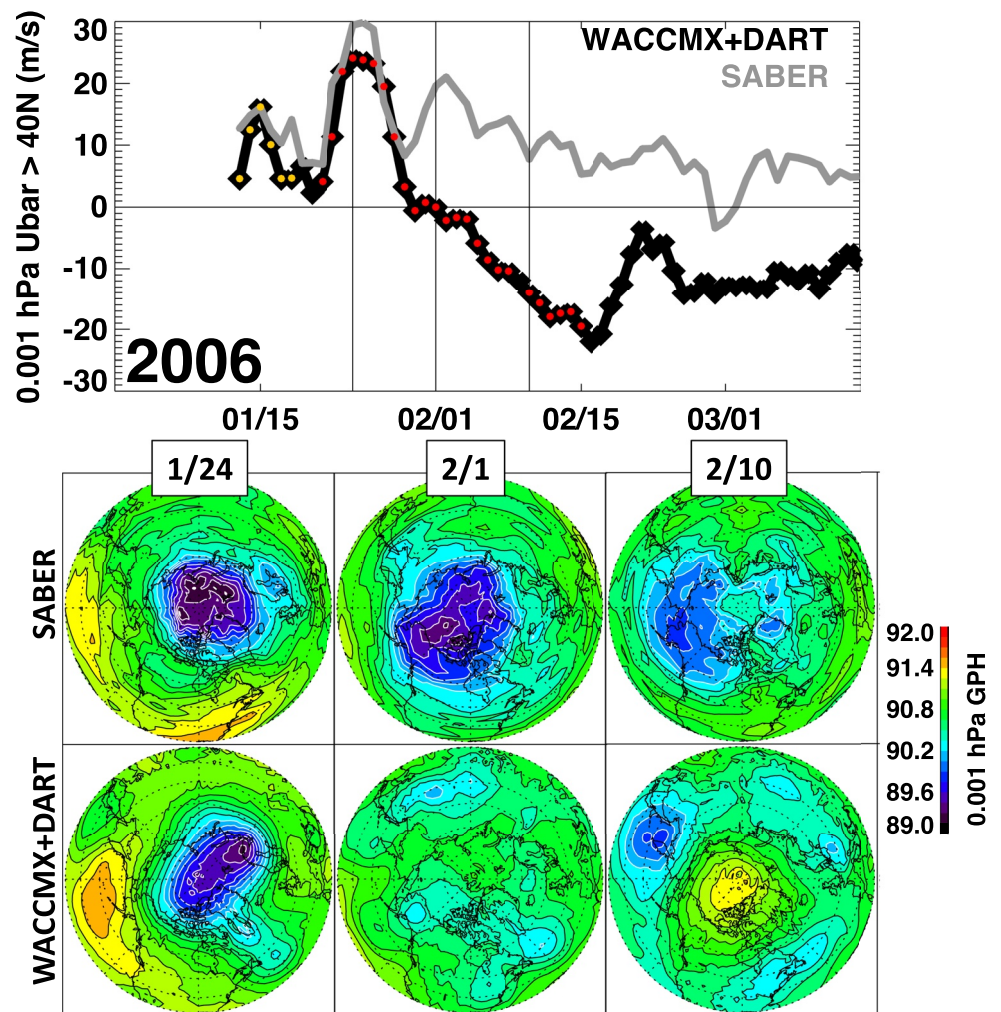
Figure 5. (top) Timeseries of WACCMX+DART (black) and Sounding of the Atmosphere using Broadband Emission Radiometry (SABER) (gray) daily average zonal mean zonal winds from 40° to 90°N at 0.001 hPa (~90 km) from 13 January to 15 March 2006. (Middle and bottom rows) Northern Hemisphere polar plots of daily average geopotential height (GPH) at 0.001 hPa in SABER (middle row) and WACCMX+DART (bottom row) on 24 January, 1 February, and 10 February 2006. The dates of these three polar plots is indicated by the vertical lines in the timeseries. A major sudden stratospheric warming began on 21 January.

has been associated with dynamical variability at stratopause altitudes (e.g., Limpasuvan et al., 2016; Stray et al., 2015; Tweedy et al., 2013). One reason for this is that due to shorter radiative relaxation time-scales at higher altitudes (e.g., Andrews et al., 1987), it takes less time for stratopause winds to recover after a SSW than it does for winds at 10 hPa. Days with easterlies at 0.6 hPa are indicated by blue diamonds in Figure 6; they occur during both minor and major SSWs and they are confined to the initial part of prolonged major SSWs. Table 2 compares means and standard deviations in model and observed zonal wind speeds for different levels of disturbances, including periods that are defined to coincide with minor or major SSWs in accordance with winds and temperatures at 10 hPa, as well as periods when the zonal mean zonal wind at 0.6 hPa (near the stratopause) is easterly (77 days). For the aforementioned reason, in a mean sense, the model winds are in closest agreement with the observations during minor SSWs or when the zonal wind at the stratopause is easterly.

Figure 7 presents the same information shown in Figure 6 but as scatterplots. The difference between Figures 7a and 7b is the red dots indicate easterlies at 10 hPa in Figure 7a versus easterlies at the stratopause (0.6 hPa, ~55 km) in Figure 7b. On non-SSW days most black points are clustered in the upper left quadrant where the simulated zonal winds are negative (easterly) and observed zonal winds are positive (westerly). During minor and major SSWs, points are often in the upper right quadrant where both simulated and observed winds are westerly.
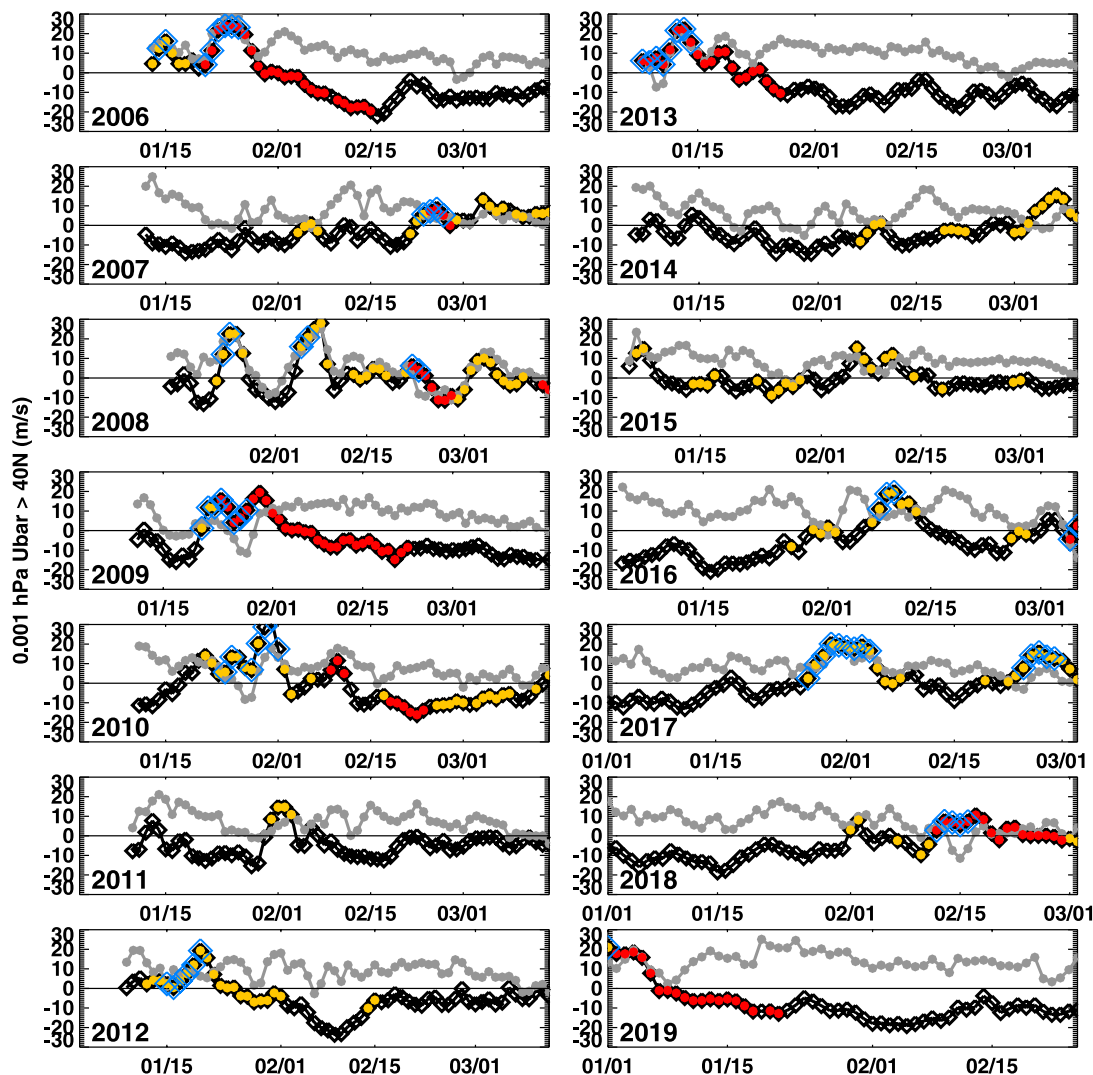
Figure 6. Timeseries of WACCMX+DART (black with diamonds) and Sounding of the Atmosphere using Broadband Emission Radiometry (SABER) (gray) 0.001 hPa daily average zonal mean zonal winds poleward of 40°N for each January-March northern SABER yaw from 2006 to 2019. Days that satisfy minor and major sudden stratospheric warming conditions are indicated with yellow and red dots, respectively. Days with easterlies near the stratopause (0.6 hPa) are indicated with blue diamonds.

Table 2
Mean Zonal Wind and 1-Standard Deviation in WACCMX+DART and SABER in the NH (Data Shown in Figure 6) and SH (Data Shown in Figure 9) For All Days, Non-SSW Days, Minor SSW Days, and Major SSW Days. Zonal Wind Is at 0.001 hPa (~90 km) and Is Averaged in Broad Latitude Bands Poleward of 40°N (For the NH) or 40°S (For the Southern Hemisphere (SH)).

	Hemisphere and Model/Obs	All	Non-SSW	Minor SSW	Major SSW	0.6 hPa U<0
Figure 6	NH Model U (1-sigma)	-3.3 (9.1)	-7.1 (6.4)	4.5 (8.6)	0.6 (10.1)	12.6 (7.4)
	NH SABER U (1-sigma)	8.4 (6.3)	8.8 (5.5)	7.0 (5.9)	8.7 (8.9)	7.7 (9.8)
Figure 9	SH Model U (1-sigma)	-7.2 (4.6)	-7.2 (4.6)	N/A	N/A	N/A
	SH SABER U (1-sigma)	17.5 (5.5)	17.5 (5.5)			

Note. Northern Hemisphere (NH); Southern Hemisphere (SH); Sounding of the Atmosphere Using Broadband Emission Radiometry (SABER); Sudden Stratospheric Warming (SSW).
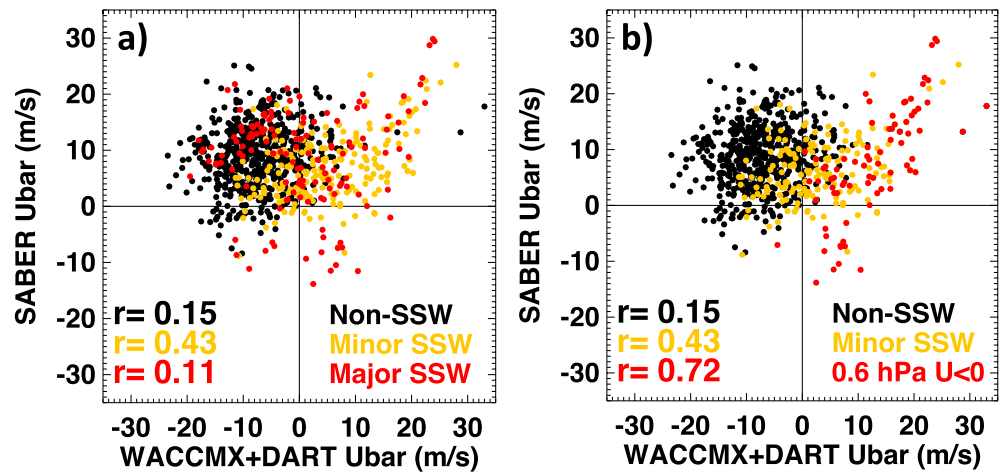
Figure 7. Scatterplot of all WACCMX+DART versus Sounding of the Atmosphere using Broadband Emission Radiometry (SABER) zonal mean zonal wind data presented in Figure 6. (a) Days that satisfy minor and major sudden stratospheric warming (SSW) conditions are indicated with yellow and red dots, respectively. (b) as panel (a) but red dots indicate easterlies at 0.6 hPa instead of at 10 hPa.

Figure 7a shows a population of red points in the upper left quadrant; these points represent days discussed above that occur 2–4 weeks after major SSW onset. Figure 7b reveals that much higher correlation (0.72) between WACCMX+DART and SABER zonal winds in the upper mesosphere is achieved for days when zonal winds at the stratopause are easterly. In this case, the correlation between modeled and observed MLT winds steadily increases from non-SSW days, to minor SSW days, to days with easterlies at the stratopause.

Next it will be shown that the time variation in model winds in the MLT is largely driven by modulation of the polar night jet in the USLM, as expected due to GW filtering and dissipation processes. Figure 8a shows the correlation coefficient between model-measurement wind *differences* near 90 km ($\sim10^{-3}$ hPa; top horizontal black line) and WACCMX+DART zonal winds at other altitudes. Wind differences at 0.001 hPa (~90 km) are highly positively correlated with zonal winds at the same altitude. However, the vertical profile of the correlation coefficient indicates that wind differences near 90 km are highly negatively correlated ($r = -0.79$) with zonal winds in the USLM (~0.6 hPa, ~55 km). Figure 8b shows a timeseries of model-measurement zonal wind differences poleward of 40°N in the upper mesosphere at 0.001 hPa (thick black contour) for all years combined. The timeseries of zonal winds in the USLM is overplotted in blue, referenced to the right vertical axis; this is the altitude where the negative correlation with the 0.001 hPa wind differences maximizes. Note, the blue y-axis
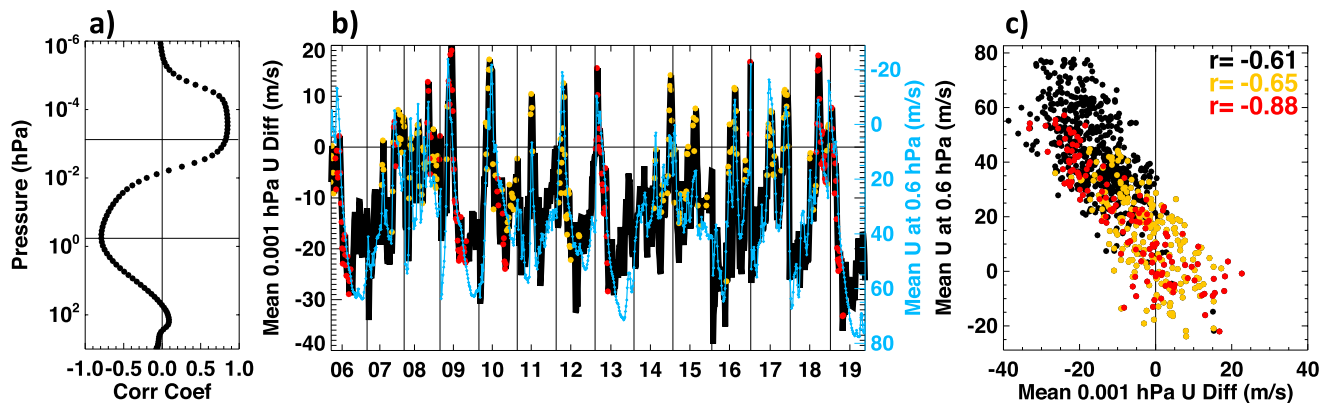

Figure 8. (a) Vertical profile of the correlation coefficient between wind differences at 0.001 hPa (~90 km at the altitude indicated by top horizontal line) and zonal mean winds at other altitudes. (b) timeseries of daily average zonal mean zonal wind differences (WACCMX+DART minus SABER) poleward of 40°N near 90 km (thick black). Superimposed in blue is the timeseries of zonal mean zonal wind poleward of 40°N in the lower mesosphere (0.6 hPa, near 55 km and indicated by the bottom horizontal black line in panel a where the correlation minimizes). (c) Scatterplot of data presented in panel b (note, the y-axis is reversed compared to the right y-axis in panel b, to emphasize negative correlation). Days with minor and major SSWs are indicated with yellow and red dots, respectively.
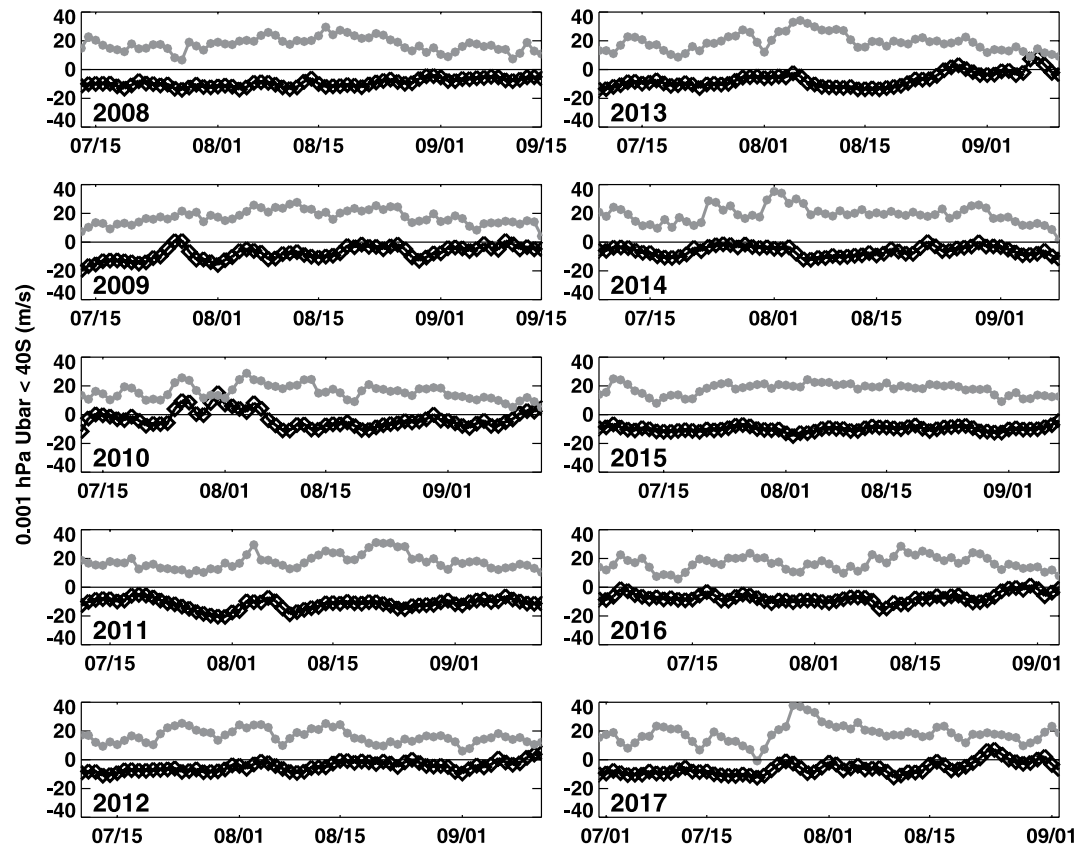
Figure 9. Timeseries of WACCMX+DART (black with diamonds) and Sounding of the Atmosphere using Broadband Emission Radiometry (gray) 0.001 hPa daily average zonal mean zonal winds poleward of 40°S for each June-September southern SABER yaw from 2008 to 2017.

ranges from positive at the bottom to negative at the top, so overlap between the black and blue curves indicates that they are anticorrelated. This analysis reveals that model-measurement *differences* in zonal winds in the MLT are highly negatively correlated with the zonal wind itself in the USLM. These results also indicate that the model is in better agreement with the observations (differences are close to zero) during SSWs, when zonal winds in the stratosphere weaken or reverse direction (with the notable exception of 2–4 weeks following major SSW onset). As will be discussed later, the time variation in model-measurement differences is largely driven by variations in non-orographic GW drag. Figure 8c shows a scatterplot of data shown in Figure 8b. This analysis demonstrates that the model easterly wind bias (points to the left of zero) is reduced as the zonal winds in the USLM weaken, as expected (e.g., McLandress et al., 2013). Interestingly, periods during which the 0.6 hPa wind is weaker than ~+20 m/s or easterly are the only times when the zonal mean zonal wind in the model is on average greater (more westerly) than in the observations. And most (115/124 = 93%) of these days are also a minor or major SSW day. The anticorrelation between model-measurement wind differences near the mesopause and zonal winds near the stratopause increases from non-SSW days ($r = −0.61$) to minor SSW days ($r = −0.65$) to major SSW days ($r = −0.88$). These results indicate that model-measurement differences at the mesopause are anticorrelated with USLM winds regardless of dynamical activity but even more so during SSWs. In other words, the easterly model wind bias in the upper mesosphere is largest when USLM zonal winds are strong and is smallest when USLM winds are weak. This suggests that the strength of the polar night jet in the USLM is a useful proxy for model fidelity in the Arctic polar winter MLT.

4.2. Southern Hemisphere Winter

Now we turn our attention to the Antarctic. Figure 9 shows ten June-September segments for each year from 2008 to 2017 of WACCMX+DART and SABER daily averaged zonal mean zonal winds at 0.001 hPa for all
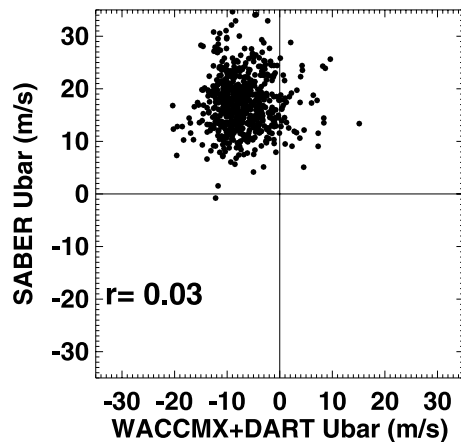
Figure 10. Scatterplot of all WACCMX+DART versus Sounding of the Atmosphere using Broadband Emission Radiometry (SABER) zonal mean zonal wind data presented in Figure 9.

days (649) in which SABER observed the SH. WACCMX+DART (black with diamonds) and SABER (gray) zonal winds are averaged in a broad latitude range poleward of 40°S to assess the largest spatial scales. No minor or major SSW days are identified for the dates included in this study. The lack of SSWs largely reflects that the SABER observations are confined to the winter season and do not extend into spring. Similar to the NH, the model and observed zonal winds are uncorrelated ($r = 0.03$) at this altitude based on all 649 days. A notable difference, compared to the NH, is that the observed winds are 2× stronger. Also, the model winds in the SH MLT do not exhibit as much sub-seasonal or interannual variability as in the NH. Instead, easterly winds persist when the Antarctic vortex is strong, consistent with the easterly wind bias seen in the NH for non-SSW days. These points are reflected in the timeseries shown in Figure 9 in that the black and gray curves hardly ever overlap. The most significant overlap occurs in late July 2010 during which time the polar night jet weakened but neither the winds nor the meridional temperature gradient reversed (see Eswaraiah et al., 2016 their Figure 1). See Table 2 for means and standard deviations in modeled and observed zonal wind speeds for all days (which is equal to non-SSW days). Figure 10 presents the same information as shown in Figure 9 but as a scatterplot. Here most points are clustered in the upper left quadrant, where modeled zonal winds are negative and observed zonal winds are positive. The distribution of black points is similar to non-SSW points in the NH.

Next we explore the relationship between the persistent easterly model wind bias in the SH MLT and the strength of the polar night jet in the USLM. Figure 11 is as Figure 8 but for the SH. Figure 11a shows that the shape of the vertical profile in the correlation coefficient (between model-measurement wind *differences* at 0.001 hPa and WACCMX+DART winds at other altitudes) is similar in both hemispheres. As is true in the NH, the model-measurement differences at 0.001 hPa are negatively correlated ($r = -0.59$) with zonal winds in the USLM, with a maximum anti-correlation near the stratopause at 0.6 hPa. Figure 11b demonstrates that the easterly wind bias is, on average, over 2× larger in the SH (-26.3 m/s) than in the NH (-11.6 m/s). Despite this, it is important to note that similar to the NH, this bias is reduced (the black line is closer to zero) when zonal winds near the stratopause weaken. Figure 11c shows a scatterplot of the timeseries shown in Figure 11b. This perspective confirms that the model easterly wind bias (that the points are on the left side) is reduced as the zonal winds in the USLM weaken. Thus, despite the persistence of a model easterly wind bias in the Antarctic, and in the Arctic during strong vortex periods, the strength of the zonal winds in the USLM can be used to infer model fidelity in the polar winter MLT.
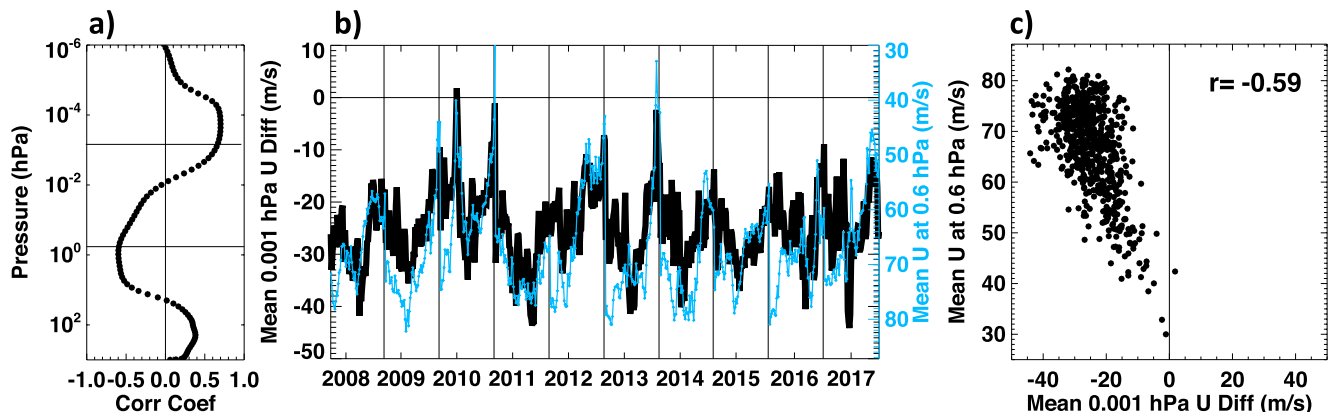

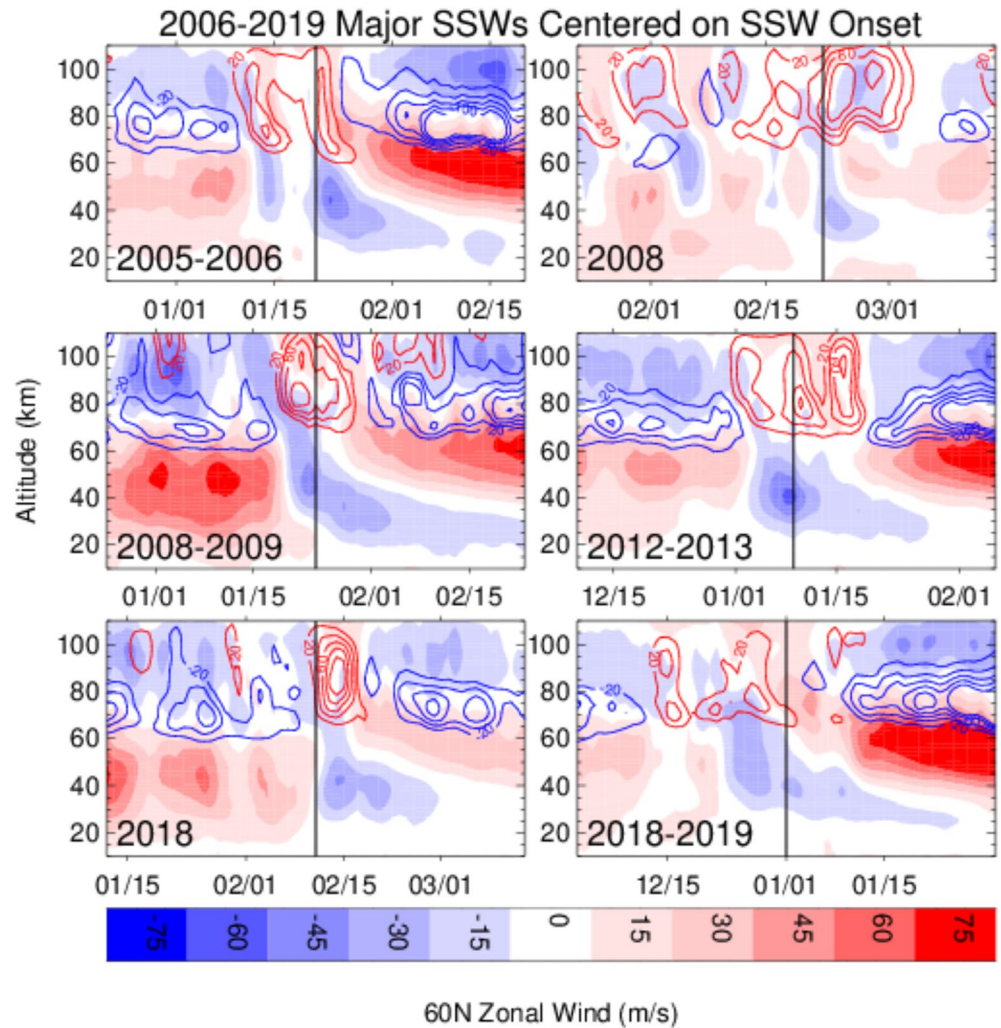**Figure 11.** As Figure 8 except for in the Southern Hemisphere.

Figure 12. Altitude-time sections of daily average zonal mean zonal wind from WACCMX+DART at 60°N (color fill) for six major SSWs. Superimposed is the zonal wind acceleration (m/s/day) imparted by gravity waves with frontal sources (contours). Major SSWs are shown for (a) January 2006, (b) February 2008, (c) January 2009, (d) January 2013, (e) February 2018, and (f) January 2019. See Table 1 for onset dates associated with the vertical black lines. The x-axis range from ±30 days from sudden stratospheric warming (SSW) onset.

5. Discussion

Variability in model winds in the winter MLT is consistent with the time variation in parameterized GW drag, as expected given GW filtering and dissipation processes (e.g., Limpasuvan et al., 2016; see their Figure 4b and discussion thereof). In the polar winter, GW drag due to convective GWs is negligible; GWs with frontal sources impart an order of magnitude larger drag than orographic GWs, since GWs with frontal sources propagate to higher altitudes than orographic GWs (not shown). As a result, hereafter we focus on GW drag from non-orographic GWs with frontal sources. It is well known that GWs with phase speeds opposite to the stratospheric winds are able to propagate to the mesosphere and deposit momentum that drives a poleward residual circulation (Holton, 1983) and induces the separated polar winter stratopause (Hitchman et al., 1989). According to thermal wind balance, this gives rise to weaker westerly winds, or even easterly winds, when compared to a state with no GW drag in the winter stratosphere and mesosphere.

Figure 12 gives altitude-time sections of WACCMX+DART zonal mean zonal wind (color fill) and frontal GW drag (contours) centered on 6 major SSWs (±30 days). In general, GW drag in the MLT and the stratospheric zonal wind are in opposite directions. When the stratospheric zonal wind is westerly (red shades), GWs impart

strong westward drag in the MLT (blue contours); the reverse is also true. This westward GW drag prior to and well after an SSW results in easterly MLT winds. But when the stratospheric zonal winds are reduced or reversed to easterly (blue shades) during SSWs, westward GWs are filtered or dissipate in the lower stratosphere. This results in a net propagation of eastward primary non-orographic GWs into the MLT, which leads to eastward drag (red contours). This result is consistent with Pedatella, Smith, and Liu (2018, see their Figure 6), who showed that a weakening of the polar night jet in the SH led to enhancements in parameterized eastward GW drag in the upper mesosphere.

Given the results in Figure 12, a plausible explanation for the larger easterly wind bias in the model MLT during dynamically quiet (strong vortex) times is as follows. We hypothesize that the westward drag, and thus easterly wind, in the MLT is overestimated because WACCMX+DART does not include secondary or higher order GWs, and that the errors associated with this GW deficiency are more important during dynamically quiet times when the vortex is strong and stable. When quasi-stationary PW forcing from the troposphere is weak, the polar night jet is strong and westerly. This scenario allows primary GWs with westward phase speeds to propagate to the mesosphere, break, and deposit their momentum, thus reversing the direction of the winter westerly jet. When these waves break, they launch a spectrum of secondary GWs in various directions (Vadas, 2013; Vadas et al., 2018). Since winds above the breaking region become more easterly with altitude, only the GWs that propagate eastward relative to the mean flow can reach the MLT, where they dissipate as a result of the strong wind variations associated with the semidiurnal tide (Becker & Vadas, 2018, their Figure 13). Specifically, Figure 13 in Becker and Vadas (2018) shows that the dissipation of eastward secondary GWs is strongest when the zonal tidal wind component shifts from westward to eastward (when du/dt maximizes). It is the tidal wind oscillating in time that is responsible for the crucial dependence of GW dissipation on the semidiurnal tide (Becker, 2017). This secondary GW dissipation imparts strong eastward drag, so the net effect is to induce eastward (positive) vertical wind shear in the upper mesosphere, leading to westerly mean winds. If secondary GWs are omitted from the model, their eastward drag cannot contribute to the MLT winds, which therefore assume an easterly bias. Furthermore, westward primary GWs propagate to higher altitudes and impart stronger drag when the vortex is stronger and more stable (e.g., Becker & Schmitz, 2003), and the GW amplitudes increase as the breaking altitude of primary GWs increases (Vadas & Becker, 2019; Vadas et al., 2003, 2018). Following arguments of Vadas & Becker (2019), we expect stronger secondary GW activity when the vortex is stronger and less variable, as demonstrated by Becker et al. (2020) using the GW-resolving model of Becker and Vadas (2018). Thus the effect of excluding secondary GWs is more significant when the polar vortex is strong.

6. Conclusions

It is well known that WACCM and other high-top general circulation models exhibit a strong easterly (westward) zonal wind bias in the polar winter upper mesosphere. Here we show for the first time that this easterly zonal wind bias in the model varies throughout the winter in accordance with dynamical forcing from below. Comparisons between WACCMX+DART and SABER demonstrate that the model zonal winds in the MLT are in closer agreement with the observations when zonal winds in the USLM are weak, often during major and minor SSW events.

The mechanism responsible for modulation of the model easterly wind bias in the MLT is that a weakening or reversal of the stratospheric and mesospheric polar night jet allows primary non-orographic GWs to propagate into the MLT, which drives eastward vertical wind shear, resulting in zonal winds in the MLT that are in agreement with the observations. Since observed MLT westerly zonal winds are on average stronger in the SH than in the NH, and since the stratospheric polar night jet in the SH is stronger than in the NH, this results in a persistent model wind bias in the polar winter MLT that is 2× larger in the SH than in the NH. In both hemispheres results shown here indicate that the polar night jet speed near the stratopause may be a useful proxy for model fidelity in the polar winter MLT.

One explanation for the model easterly wind bias in the polar winter MLT is that the model omits higher order GWs, and thus the eastward drag caused by these GWs. Other known deficiencies in the existing GW parameterization that may contribute to the easterly wind bias in the model include: the absence of oblique GW propagation (e.g., Sato et al., 2009; Thurairajah et al., 2017, 2020), the need to modify the GW source spectrum (e.g., Liu & Roble, 2002; Pramitha et al., 2020), the need to impose GW sources at all altitudes (e.g., Ribstein et al., 2022) including tropospheric jet exit regions and the stratospheric polar vortex (e.g., Becker et al., 2022; Dörnbrack

et al., 2018; Sato & Yoshiki, 2008), and the need to tune GW parameterizations according to simulated tidal variability (e.g., Becker, 2017). Future work will investigate running the model at 0.25° horizontal resolution, following Liu et al. (2014), to quantify the sensitivity of the easterly wind bias to model resolution. As in Karlsson and Becker (2016), we will specifically focus on time periods of expected inter-hemispheric coupling when the polar vortex is strong, because the winter MLT wind bias is maximum during these times, and because it is of interest to make sure that model improvements in the winter hemisphere do not result in a simultaneous degradation of the summer mesopause. Our hypothesis is that increasing the horizontal and vertical resolution and using physics-based subgrid-scale diffusion (e.g., Becker & Vadas, 2020, their Appendix A) will allow the model to explicitly resolve more of the GW spectrum such that higher order GWs and their effects are accounted for and the easterly wind bias is reduced. Indeed, promising results from a version of the free-running WACCM with ~0.25° horizontal resolution (Liu, 2017, see his Figure 1) showed no easterly wind bias in the SH winter MLT at high latitudes.

Data Availability Statement

WACCMX is part of the Community Earth System Model (CESM) and the source code is available at http://www.cesm.ucar.edu. Post processed (daily zonal mean) WACCMX+DART output used to produce figures that appear in this work are provided at https://doi.org/10.5281/zenodo.6513075 (Harvey et al., 2022). SABER data are available at saber.gats-inc.com/browse_data.php#.

References

Akmaev, R. A. (2011). Whole atmosphere modeling: Connecting terrestrial and space weather. *Reviews of Geophysics*, *49*(4), RG4004. https://doi.org/10.1029/2011RG000364

Alexandre, D., Thurairajah, B., England, S. L., & Cullens, C. Y. (2021). A hemispheric and seasonal comparison of tropospheric to mesospheric gravity-wave propagation. *Journal of Geophysical Research: Atmospheres*, *126*(18), e2021JD034990. https://doi.org/10.1029/2021JD034990

Anderson, J. L. (2001). An ensemble adjustment Kalman filter for data assimilation. *Monthly Weather Review*, *129*(12), 2884–2903. https://doi.org/10.1175/1520-0493(2001)129<2884:AEAKFF>2.0.CO;2

Andrews, D. G., Holton, J. R., & Leovy, C. B. (1987). *Middle atmosphere dynamics* (1st ed.). Academic Press.

Becker, E. (2017). Mean-flow effects of thermal tides in the mesosphere and lower thermosphere. *Journal of the Atmospheric Sciences*, *74*(6), 2043–2063. https://doi.org/10.1175/JAS-D-16-0194.1

Becker, E., Grygalashvyly, M., & Sonnemann, G. R. (2020). Gravity wave mixing effects on the OH*-layer. *Advances in Space Research*, *65*(1), 175–188. https://doi.org/10.1016/j.asr.2019.09.043

Becker, E., & Schmitz, G. (2003). Climatological effects of orography and land–sea heating contrasts on the gravity wave–driven circulation of the mesosphere. *Journal of the Atmospheric Sciences*, *60*(1), 103–118. https://doi.org/10.1175/1520-0469(2003)060<0103:CEOOAL>2.0.CO;2

Becker, E., & Vadas, S. L. (2018). Secondary gravity waves in the winter mesosphere: Results from a high-resolution global circulation model. *Journal of Geophysical Research: Atmospheres*, *123*(5), 2605–2627. https://doi.org/10.1002/2017JD027460

Becker, E., & Vadas, S. L. (2020). Explicit global simulation of gravity waves in the thermosphere. *Journal of Geophysical Research: Space Physics*, *125*(10). https://doi.org/10.1029/2020JA028034

Becker, E., Vadas, S. L., Bossert, K., Harvey, V. L., Zülicke, C., & Hoffmann, L. (2022). A high-resolution whole-atmosphere model with resolved gravity waves and specified large-scale dynamics in the troposphere and lower stratosphere. *Journal of Geophysical Research: Atmospheres*, *127*(2). https://doi.org/10.1029/2021JD035018

Beres, J. H., Garcia, R. R., Boville, B. A., & Sassi, F. (2005). Implementation of a gravity wave source spectrum parameterization dependent on the properties of convection in the whole atmosphere community climate model (WACCM). *Journal of Geophysical Research*, *110*(D10), D10108. https://doi.org/10.1029/2004JD005504

Butler, A. H., Seidel, D. J., Hardiman, S. C., Butchart, N., Birner, T., & Match, A. (2015). Defining sudden stratospheric warmings. *Bulletin America Meteorology Social*, *96*(11), 1913–1928. https://doi.org/10.1175/BAMS-D-13-00173.1

Butler, A. H., Sjoberg, J. P., Seidel, D. J., & Rosenlof, K. H. (2017). A sudden stratospheric warming compendium. *Earth System Science Data*, *9*(1), 63–76. https://doi.org/10.5194/essd-9-63-2017

Chandran, A., Garcia, R. R., Collins, R. L., & Chang, L. C. (2013). Secondary planetary waves in the middle and upper atmosphere following the stratospheric sudden warming event of January 2012. *Geophysical Research Letters*, *40*(9), 1861–1867. https://doi.org/10.1002/grl.50373

Charney, J. G., & Stern, M. E. (1962). On the stability of internal baroclinic jets in a rotating atmosphere. *Journal of the Atmospheric Sciences*, *19*(2), 159–172. https://doi.org/10.1175/1520-0469(1962)019<0159:OTSOIB>2.0.CO;2

Datta-Barua, S., Pedatella, N., Greer, K. R., Wang, N., Nutter, L., & Harvey, V. L. (2021). Lower thermospheric material transport via Lagrangian coherent structures. *Journal of Geophysical Research: Space Physics*, *126*(9). https://doi.org/10.1029/2020JA028834

Dörnbrack, A., Gisinger, S., Kaifler, N., Portele, T. C., Bramberger, M., Rapp, M., et al. (2018). Gravity waves excited during a minor sudden stratospheric warming. *Atmospheric Chemistry and Physics*, *18*(17), 12915–12931. https://doi.org/10.5194/acp-18-12915-2018

Eswaraiah, A., Kim, Y. H., Hong, J., Kim, J.-H., Venkat Ratnam, M., Chandran, A., et al. (2016). Mesospheric signatures observed during 2010 minor stratospheric warming at King Sejong Station (62°S, 59°W). *Journal of Atmospheric and Solar-Terrestrial Physics*, *140*, 55–64. https://doi.org/10.1016/j.jastp.2016.02.007

France, J. A., Harvey, V. L., Randall, C. E., Collins, R. L., Smith, A. K., Peck, E. D., & Fang, X. (2015). A climatology of planetary wave-driven mesospheric inversion layers in the extratropical winter. *Journal of Geophysical Research: Atmospheres*, *120*(2), 399–413. https://doi.org/10.1002/2014JD022244

Fritts, D., & Luo, Z. (1992). Gravity wave excitation by geostrophic adjustment of the jet stream, part 1: Two-dimensional forcing. *Journal of the Atmospheric Sciences*, *49*(8), 681–697. https://doi.org/10.1175/1520-0469(1992)049<0681:GWEBGA>2.0.CO;2

Froidevaux, L., Kinnison, D. E., Wang, R., Anderson, J., & Fuller, R. A. (2019). Evaluation of CESM1 (WACCM) free-running and specified dynamics atmospheric composition simulations using global multispecies satellite data records. *Atmospheric Chemistry and Physics*, *19*(7), 4783–4821. https://doi.org/10.5194/acp-19-4783-2019

Garcia, R. R., López-Puertas, M., Funke, B., Marsh, D. R., Kinnison, D. E., Smith, A. K., & González-Galindo, F. (2014). On the distribution of CO_2 and CO in the mesosphere and lower thermosphere. *Journal of Geophysical Research - D: Atmospheres*, *119*(9), 5700–5718. https://doi.org/10.1002/2013JD021208

García-Comas, M., López-Puertas, M., Marshall, B. T., Wintersteiner, P. P., Funke, B., Bermejo-Pantaleón, D., et al. (2008). Errors in sounding of the atmosphere using broadband emission radiometry (SABER) kinetic temperature caused by non-local-thermodynamic equilibrium model parameters. *Journal of Geophysical Research*, *113*(D24), D24106. https://doi.org/10.1029/2008JD010105

Griffith, M. J., Dempsey, S. M., Jackson, D. R., Moffat-Griffin, T., & Mitchell, N. J. (2021). Winds and tides of the Extended Unified Model in the mesosphere and lower thermosphere validated with meteor radar observations. *Annales Geophysicae*, *39*(3), 487–514. https://doi.org/10.5194/angeo-39-487-2021

Harvey, V. L., Pedatella, N., Becker, E., & Randall, C. E. (2022). Evaluation of polar winter mesopause wind in WACCMX+DART [Data Set]. Zenodo. https://zenodo.org/record/6513075

Harvey, V. L., Randall, C. E., Becker, E., Smith, A. K., Bardeen, C. G., France, J. A., & Goncharenko, L. P. (2019). Evaluation of the mesospheric polar vortices in WACCM. *Journal of Geophysical Research: Atmospheres*, *124*(20), 10626–10645. https://doi.org/10.1029/2019JD030727

Hindley, N. P., Cobbett, N., Fritts, D. C., Janchez, D., Mitchell, N. J., Moffat-Griffin, T., et al. (2022). Radar observations of winds, waves and tides in the mesosphere and lower thermosphere over South Georgia island (54°S, 36°W) and comparison to WACCM simulations. *Atmospheric Chemistry and Physics*. https://doi.org/10.5194/acp-2021-981

Hitchman, M. H., Gille, J. C., Rodgers, C. D., & Brasseur, G. (1989). The separated polar winter stratopause: A gravity wave driven climatological feature. *Journal of the Atmospheric Sciences*, *46*(3), 410–422. https://doi.org/10.1175/1520-0469(1989)046<0410:TSPWSA>2.0.CO;2

Holton, J. R. (1983). The influence of gravity wave breaking on the general circulation of the middle atmosphere. *Journal of the Atmospheric Sciences*, *40*(10), 2497–2507. https://doi.org/10.1175/1520-0469(1983)040<2497:TIOGWB>2.0.CO;2

Holton, J. R. (2004). *An introduction to dynamic meteorology* (4th ed.). Elsevier Academic Press.

Kalisch, S., Preusse, P., Ern, M., Eckermann, S. D., & Riese, M. (2014). Differences in gravity wave drag between realistic oblique and assumed vertical propagation. *Journal of Geophysical Research: Atmospheres*, *119*(17), 10081–10099. https://doi.org/10.1002/2014JD021779

Karlsson, B., & Becker, E. (2016). How does interhemispheric coupling contribute to cool down the summer polar mesosphere? *Journal of Climate*, *29*(24), 8807–8821. https://doi.org/10.1175/JCLI-D-16-0231.1

Knuth, D. E. (1992). *Axioms and hulls*. Springer. https://doi.org/10.1007/3-540-55611-7

Larsen, M. F. (2002). Winds and shears in the mesosphere and lower thermosphere: Results from four decades of chemical release wind measurements. *Journal of Geophysical Research*, *107*(A8), 1215. https://doi.org/10.1029/2001JA000218

Lieberman, R. S., Fritts, D. C., Pedatella, N., Doornbos, E., & Ortland, D. A. (2015). Global observations of thermospheric lunar tidal winds. *Journal of Atmospheric and Solar-Terrestrial Physics*, *136*, 126–133. https://doi.org/10.1016/j.jastp.2015.05.019

Lieberman, R. S., Riggin, D. M., & Siskind, D. E. (2013). Stationary waves in the wintertime mesosphere: Evidence for gravity wave filtering by stratospheric planetary waves. *Journal of Geophysical Research: Atmospheres*, *118*(8), 3139–3149. https://doi.org/10.1002/jgrd.50319

Limpasuvan, V., Orsolini, Y. J., Chandran, A., Garcia, R. R., & Smith, A. K. (2016). On the composite response of the MLT to major sudden stratospheric warming events with elevated stratopause. *Journal of Geophysical Research: Atmospheres*, *121*(9), 4518–4537. https://doi.org/10.1002/2015JD024401

Liu, H.-L. (2007). On the large wind shear and fast meridional transport above the mesopause. *Geophysical Research Letters*, *34*(8), L08815. https://doi.org/10.1029/2006GL028789.s

Liu, H.-L. (2016). Variability and predictability of the space environment as related to lower atmosphere forcing. *Space Weather*, *14*(9), 634–658. https://doi.org/10.1002/2016SW001450

Liu, H.-L. (2017). Gravity wave variation from the troposphere to the lower thermosphere during a stratospheric sudden warming event: A case study. *Scientific Online Letters on the Atmosphere (SOLA)*, *13A*, 24–30. https://doi.org/10.2151/sola.13A-005

Liu, H.-L., Bardeen, C. G., Foster, B. T., Lauritzen, P., Liu, J., Lu, G., et al. (2018). Development and validation of the whole atmosphere community climate model with thermosphere and ionosphere extension (WACCM-X 2.0). *Journal of Advances in Modeling Earth Systems*, *10*(2), 381–402. https://doi.org/10.1002/2017MS001232

Liu, H.-L., McInerney, J. M., Santos, S., Lauritzen, P. H., Taylor, M. A., & Pedatella, N. M. (2014). Gravity waves simulated by high-resolution whole atmosphere community climate model. *Geophysical Research Letters*, *41*(24), 9106–9112. https://doi.org/10.1002/2014GL062468

Liu, H.-L., & Roble, R. G. (2002). A study of a self-generated stratospheric sudden warming and its mesospheric – Lower thermospheric impacts using the coupled TIME-GCM/CCM3. *Journal of Geophysical Research*, *107*(D23), 4695. https://doi.org/10.1029/2001JD001533

Manney, G. L., Krüger, K., Pawson, S., Minschwaner, K., Schwartz, M. J., Daffer, W. H., et al. (2008). The evolution of the stratopause during the 2006 major warming: Satellite data and assimilated meteorological analyses. *Journal of Geophysical Research*, *113*(D11), D11115. https://doi.org/10.1029/2007JD009097

Marsh, D. R., Mills, M. J., Kinnison, D. E., Lamarque, J. F., Calvo, N., & Polvani, L. M. (2013). Climate change from 1850 to 2005 simulated in CESM1 (WACCM). *Journal of Climate*, *26*(19), 7372–7391. https://doi.org/10.1175/JCLI-D-12-00558.1

McCormack, J., Hoppel, K., Kuhl, D., de Wit, R., Stober, G., Espy, P., et al. (2017). Comparison of mesospheric winds from a high-altitude meteorological analysis system and meteor radar observations during the boreal winters of 2009–2010 and 2012–2013. *Journal of Atmospheric and Solar-Terrestrial Physics*, *154*, 132–166. https://doi.org/10.1016/j.jastp.2016.12.007

McCormack, J. P., Harvey, V. L., Randall, C. E., Pedatella, N., Koshin, D., Sato, K., et al. (2021). Intercomparison of middle atmospheric meteorological analyses for the Northern Hemisphere winter 2009–2010. *Atmospheric Chemistry and Physics*, *21*(23), 17577–17605. https://doi.org/10.5194/acp-21-17577-2021

McFarlane, N. A. (1987). The effect of orographically excited wave drag on the general circulation of the lower stratosphere and troposphere. *Journal of the Atmospheric Sciences*, *44*(14), 1775–1800. https://doi.org/10.1175/1520-0469(1987)044<1775:TEOOEG>2.0.CO;2

McLandress, C., Scinocca, J. F., Shepherd, T. G., Reader, M. C., & Manney, G. L. (2013). Dynamical control of the mesosphere by orographic and nonorographic gravity wave drag during the extended northern winters of 2006 and 2009. *Journal of the Atmospheric Sciences*, *70*(7), 2152–2169. https://doi.org/10.1175/JAS-D-12-0297.1s

McLandress, C., Ward, W. E., Fomichev, V. I., Semeniuk, K., Beagley, S. R., McFarlane, N. A., & Shepherd, T. G. (2006). Large-scale dynamics of the mesosphere and lower thermosphere: An analysis using the extended Canadian middle atmosphere model. *Journal of Geophysical Research*, *111*(D17), D17111. https://doi.org/10.1029/2005JD006776

Meraner, K., & Schmidt, H. (2016). Transport of nitrogen oxides through the winter mesopause in HAMMONIA. *Journal of Geophysical Research - D: Atmospheres*, *121*(6), 2556–2570. https://doi.org/10.1002/2015JD024136

Noble, P. E., Hindley, N. P., Wright, C. J., Cullens, C., England, S., Pedatella, N. M., et al. (2022). Interannual variability of winds in the Antarctic mesosphere and lower thermosphere over Rothera (67°S, 68°W) in radar observations and WACCM-X. *Atmospheric Chemistry and Physics Discussions*. https://doi.org/10.5194/acp-2022-150

Orsolini, Y. J., Limpasuvan, V., Pérot, K., Espy, P., Hibbins, R., Lossow, S., et al. (2017). Modelling the descent of nitric oxide during the elevated stratopause event of January 2013. *Journal of Atmospheric and Solar-Terrestrial Physics*, *155*(2017), 50–61. https://doi.org/10.1016/j.jastp.2017.01.006

Pedatella, N. M., Fuller-Rowell, T., Wang, H., Jin, H., Miyoshi, Y., Fujiwara, H., et al. (2014). The neutral dynamics during the 2009 sudden stratosphere warming simulated by different whole atmosphere models. *Journal of Geophysical Research*, *119*(2014), 1306–1324. https://doi.org/10.1002/2013JA019421

Pedatella, N. M., Liu, H.-L., Marsh, D. R., Raeder, K., Anderson, J. L., Chau, J. L., et al. (2018). Analysis and hindcast experiments of the 2009 sudden stratospheric warming in WACCMX+DART. *Journal of Geophysical Research: Space Physics*, *123*(4), 3131–3153. https://doi.org/10.1002/2017JA025107

Pedatella, N. M., Raeder, K., Anderson, J. L., & Liu, H.-L. (2013). Application of data assimilation in the Whole Atmosphere Community Climate Model to the study of day-to-day variability in the middle and upper atmosphere. *Geophysical Research Letters*, *40*(16), 4469–4474. https://doi.org/10.1002/grl.50884

Pedatella, N. M., Raeder, K., Anderson, J. L., & Liu, H.-L. (2014). Ensemble data assimilation in the whole atmosphere community climate model. *Journal of Geophysical Research - D: Atmospheres*, *119*(16), 9793–9809. https://doi.org/10.1002/2014JD021776

Pedatella, N. M., Smith, A. K., & Liu, H.-L. (2018). WACCM simulations of zonal mean gravity wave drag short-term variability in the Southern Hemisphere mesosphere. *Journal of Geophysical Research: Atmospheres*, *123*(21), 11849–11860. https://doi.org/10.1029/2018JD028306

Pérot, K., & Orsolini, Y. J. (2021). Impact of the major SSWs of February 2018 and January 2019 on the middle atmospheric nitric oxide abundance. *Journal of Atmospheric and Solar-Terrestrial Physics*, *218*, 105586. https://doi.org/10.1016/j.jastp.2021.105586

Pramitha, M., Kumar, K. K., Ratnam, M. V., Praveen, M., & Rao, S. V. B. (2020). Gravity wave source spectra appropriation for mesosphere lower thermosphere using meteor radar observations and GROGRAT model simulations. https://doi.org/10.1029/2020GL089390

Randall, C. E., Harvey, V. L., Holt, L. A., Marsh, D. R., Kinnison, D., Funke, B., & Bernath, P. F. (2015). Simulation of energetic particle precipitation effects during the 2003-2004 arctic winter. *Journal of Geophysical Research: Space Physics*, *120*(6), 5035–5048. https://doi.org/10.1002/2015JA021196

Remsberg, E., Lingenfelser, G., Harvey, V. L., Grose, W., Russell, J. M., III, Mlynczak, M., et al. (2003). On the verification of the quality of SABER temperature, geopotential height, and wind fields by comparison with Met Office assimilated analyses. *Journal of Geophysical Research*, *108*(D20), 4628. https://doi.org/10.1029/2003JD003720

Remsberg, E. E., Marshall, B. T., García-Comas, M., Krüeger, D., Lingenfelser, G. S., Martin-Torres, J., et al. (2008). Assessment of the quality of the version 1.07 temperature-versus-pressure profiles of the middle atmosphere from TIMED/SABER. *Journal of Geophysical Research*, *113*(D17), D17101. https://doi.org/10.1029/2008JD010013

Ribstein, B., Millet, C., Lott, F., & de la Cámara, A. (2022). Can we improve the realism of gravity wave parameterizations by imposing sources at all altitudes in the atmosphere? *Journal of Advances in Modeling Earth Systems*, *14*(2), e2021MS002563. https://doi.org/10.1029/2021MS002563

Richter, J. H., Sassi, F., & Garcia, R. R. (2010). Toward a physically based gravity wave source parameterization in a general circulation model. *Journal of the Atmospheric Sciences*, *67*(1), 136–156. https://doi.org/10.1175/2009JAS3112.1

Rüfenacht, R., Baumgarten, G., Hildebrand, J., Schranz, F. M., Matthias, V., Stober, G., et al. (2018). Intercomparison of middle-atmospheric wind in observations and models. *Atmospheric Measurement Techniques*, *11*(4), 1971–1987. https://doi.org/10.5194/amt-11-1971-2018

Russell, J. M., III, Mlynczak, M. G., Gordley, L. L., Tansock, J., & Esplin, R. (1999). An overview of the SABER experiment and preliminary calibration results. *Proceedings of SPIE - The International Society for Optical Engineering*, *3756*, 277–288. https://doi.org/10.1117/12.366382

Sassi, F., Siskind, D. E., Tate, J. L., Liu, H.-L., & Randall, C. E. (2018). Simulations of the boreal winter upper mesosphere and lower thermosphere with meteorological specifications in SD-WACCM-X. *Journal of Geophysical Research*, *123*(7), 3791–3811. https://doi.org/10.1002/2017JD027782

Sato, K., Watanabe, S., Kawatani, Y., Tomikawa, Y., Miyazaki, K., & Takahashi, M. (2009). On the origins of mesospheric gravity waves. *Geophysical Research Letters*, *36*(19), L19801. https://doi.org/10.1029/2009gl039908

Sato, K., & Yoshiki, M. (2008). Gravity wave generation around the polar vortex in the stratosphere revealed by 3-hourly radiosonde observations at Syowa Station. *Journal of the Atmospheric Sciences*, *65*(12), 3719–3735. https://doi.org/10.1175/2008JAS2539.1

Schmidt, H., Brasseur, G. P., Charron, M., Manzini, E., Giorgetta, M. A., Diehl, T., et al. (2006). The HAMMONIA chemistry climate model: Sensitivity of the mesopause region to the 11-year solar cycle and CO_2 doubling. *Journal of Climate*, *19*(16), 3903–3931. https://doi.org/10.1175/JCLI3829.1

Senf, F., & Achatz, U. (2011). On the impact of middle-atmosphere thermal tides on the propagation and dissipation of gravity waves. *Journal of Geophysical Research*, *116*(D24), D24110. https://doi.org/10.1029/2011JD015794

Siskind, D. E., Eckermann, S. D., McCormack, J. P., Coy, L., Hoppel, K. W., & Baker, N. L. (2010). Case studies of the mesospheric response to recent minor, major, and extended stratospheric warmings. *Journal of Geophysical Research*, *115*, D00N03. https://doi.org/10.1029/2010JD014114

Siskind, D. E., Sassi, F., Randall, C. E., Harvey, V. L., Hervig, M. E., & Bailey, S. M. (2015). Is a high-altitude meteorological analysis necessary to simulate thermosphere-stratosphere coupling? *Geophysical Research Letters*, *42*(19), 8225–8230. https://doi.org/10.1002/2015GL065838

Smith, A. K. (1996). Longitudinal variations in mesospheric winds: Evidence for gravity wave filtering by planetary waves. *Journal of the Atmospheric Sciences*, *53*(8), 1156–1173. https://doi.org/10.1175/1520-0469(1996)053<1156:LVIMWE>2.0.CO;2

Smith, A. K. (1997). Stationary planetary waves in upper mesospheric winds. *Journal of the Atmospheric Sciences*, *54*(16), 2129–2145. https://doi.org/10.1175/1520-0469(1997)054<2129:SPWIUM>2.0.CO;2

Smith, A. K. (2012). Global dynamics of the MLT. *Surveys in Geophysics*, *33*(6), 1177–1230. https://doi.org/10.1007/s10712-012-9196-9

Smith, A. K., Garcia, R. R., Marsh, D. R., & Richter, J. H. (2011). WACCM simulations of the mean circulation and trace species transport in the winter mesosphere. *Journal of Geophysical Research*, *116*(D20), D20115. https://doi.org/10.1029/2011JD016083

Smith, A. K., Pedatella, N. M., Marsh, D. R., & Matsuo, T. (2017). On the dynamical control of the mesosphere-lower thermosphere by the lower and middle atmosphere. *Journal of the Atmospheric Sciences*, *74*(3), 933–947. https://doi.org/10.1175/jas-d-16-0226.1

Smith-Johnsen, C., Marsh, D. R., Smith, A. K., Tyssøy, H. N., & Maliniemi, V. (2022). Mesospheric nitric oxide transport in WACCM. *Journal of Geophysical Research: Space Physics*, *127*(3), e2021JA029998. https://doi.org/10.1029/2021JA029998

Stevens, M. H., Lossow, S., Siskind, D. E., Meier, R., Randall, C. E., Russell, J. M., III, et al. (2014). Space shuttle exhaust plumes in the lower thermosphere: Advective transport and diffusive spreading. *Journal of Atmospheric and Solar-Terrestrial Physics*, *108*, 50–60. https://doi.org/10.1016/j.jastp.2013.12.004

Stray, N. H., Orsolini, Y. J., Espy, P. J., Limpasuvan, V., & Hibbins, R. E. (2015). Observations of planetary waves in the mesosphere-lower thermosphere during stratospheric warming events. *Atmospheric Chemistry and Physics*, *15*(9), 4997–5005. https://doi.org/10.5194/acp-15-4997-2015

Thurairajah, B., Cullens, C. Y., Siskind, D. E., Hervig, M. E., & Bailey, S. M. (2020). The role of vertically and obliquely propagating gravity waves in influencing the polar summer mesosphere. *Journal of Geophysical Research: Atmospheres*, *125*(9), e2020JD032495. https://doi.org/10.1029/2020jd032495

Thurairajah, B., Siskind, D. E., Bailey, S. M., Carstens, J. N., Russell, J. M., III, & Mlynczak, M. G. (2017). Oblique propagation of monsoon gravity waves during the northern hemisphere 2007 summer. *Journal of Geophysical Research: Atmospheres*, *122*(10), 5063–5075. https://doi.org/10.1002/2016jd026008

Tweedy, O. V., Limpasuvan, V., Orsolini, Y. J., Smith, A. K., Garcia, R. R., Kinnison, D., et al. (2013). Nighttime secondary ozone layer during major stratospheric sudden warmings in specified-dynamics WACCM. *Journal of Geophysical Research: Atmospheres*, *118*(15), 8346–8358. https://doi.org/10.1002/jgrd.50651

Vadas, S. L. (2013). Compressible f-plane solutions to body forces, heatings, and coolings, and application to the primary and secondary gravity waves generated by a deep convective plume. *Journal of Geophysical Research*, *118*(5), 2377–2397. https://doi.org/10.1002/jgra.50163

Vadas, S. L., & Becker, E. (2018). Numerical modeling of the excitation, propagation, and dissipation of primary and secondary gravity waves during wintertime at McMurdo Station in the Antarctic. *Journal of Geophysical Research: Atmospheres*, *123*(17), 9326–9369. https://doi.org/10.1029/2017JD027974

Vadas, S. L., & Becker, E. (2019). Numerical modeling of the generation of tertiary gravity waves in the mesosphere and thermosphere during strong mountain wave events over the Southern Andes. *Journal of Geophysical Research: Space Physics*, *124*(9), 7687–7718. https://doi.org/10.1029/2019JA026694

Vadas, S. L., Fritts, D. C., & Alexander, M. J. (2003). Mechanism for the generation of secondary waves in wave breaking regions. *Journal of the Atmospheric Sciences*, *60*(1), 194–214. https://doi.org/10.1175/1520-0469(2003)060<0194:MFTGOS>2.0.CO;2

Vadas, S. L., Zhao, J., Chu, X., & Becker, E. (2018). The Excitation of secondary gravity waves from local body forces: Theory and observation. *Journal of Geophysical Research: Atmospheres*, *123*(17), 9296–9325. https://doi.org/10.1029/2017JD027970

Vincent, R. A. (2015). The dynamics of the mesosphere and lower thermosphere: A brief review. *Progress in Earth and Planetary Science*, *2*(4). https://doi.org/10.1186/s40645-015-0035-8

Wilhelm, S., Stober, G., & Brown, P. (2019). Climatologies and long-term changes in mesospheric wind and wave measurements based on radar observations at high and mid latitudes. *Annales Geophysicae*, *37*(5), 851–875. https://doi.org/10.5194/angeo-37-851-2019

Yuan, T., She, C.-Y., Krueger, D. A., Sassi, F., Garcia, R. R., Roble, R. G., et al. (2008). Climatology of mesopause region temperature, zonal wind, and meridional wind over Fort Collins, Colorado (41°N, 105°W), and comparison with model simulations. *Journal of Geophysical Research*, *113*(D3), D03105. https://doi.org/10.1029/2007JD008697

Yue, J., Liu, H.-L., Meier, R., Chang, L., Gu, S.-Y., & Russell, J. M., III. (2013). On the fast zonal transport of the STS-121 space shuttle exhaust plume in the lower thermosphere. *Journal of Atmospheric and Solar-Terrestrial Physics*, *94*, 19–27. https://doi.org/10.1016/j.jastp.2012.12.017

Zhang, J., Limpasuvan, V., Orsolini, Y. J., Espy, P. J., & Hibbins, R. E. (2021). Climatological westward-propagating semidiurnal tides and their composite response to sudden stratospheric warmings in SuperDARN and SD-WACCM-X. *Journal of Geophysical Research: Atmospheres*, *126*(3), e2020JD032895. https://doi.org/10.1029/2020JD032895